Journal of Materials Chemistry A

COMMUNICATION

View Article Online
View Journal | View Issue

Cite this: J. Mater. Chem. A, 2019, 7, 1435

Received 21st November 2018
Accepted 19th December 2018

DOI: 10.1039/c8ta11197a

rsc.li/materials-a

Asymmetric selenophene-based non-fullerene acceptors for high-performance organic solar cells†

Chao Li,‡[a] Tian Xia,‡[a] Jiali Song,[a] Huiting Fu,[a] Hwa Sook Ryu,[b] Kangkang Weng,[a] Linglong Ye,[a] Han Young Woo *[b] and Yanming Sun *[a]

Compared to thiophene-based non-fullerene acceptors (NFAs), selenophene-based NFAs have received much less attention. And organic solar cells (OSCs) based on selenophene-containing NFAs typically exhibit relatively low power conversion efficiency (PCE < 12%) and fill factor (FF < 70%). In this contribution, we have designed and synthesized two asymmetric selenophene-based NFAs, named SePTT-2F and SePTTT-2F, which possess the same end-capping group but different selenophene-containing conjugated backbones. On comparing the two NFAs, SePTTT-2F with more extended conjugation in the backbone was found to have almost the same maximum absorption peak and optical bandgap in film as SePTT-2F but an up-shifted lowest unoccupied molecular orbital (LUMO) energy level and higher electron mobility. By pairing the NFAs with the polymer donor PBT1-C, the resultant blend film based on SePTTT-2F exhibited higher and more balanced charge mobilities and more efficient exciton dissociation and charge collection in comparison with the SePTT-2F-based blend film. As a result, OSCs based on SePTTT-2F delivered an impressively high PCE of 12.24% with an outstanding FF of 75.9%, much higher than those of the SePTT-2F-based OSCs. To the best of our knowledge, the PCE of 12.24% and FF of 75.9% are among the highest values reported in the literature so far for both the parameters amongst selenophene-containing NFA-based OSCs. Our results demonstrate that extending the conjugation in the selenophene-containing backbone is an effective strategy to design highly efficient selenophene-based NFAs.

Introduction

In recent years, organic solar cells (OSCs) based on blends of polymer donors and acceptor–donor–acceptor (A–D–A)-type non-fullerene acceptors (NFAs) have aroused tremendous research interest.[1–11] To date, power conversion efficiencies (PCEs) of single-junction OSCs in the range of 10–14% have been achieved, largely supported by the rapid development of a variety of A–D–A-type NFAs.[12–25] In most cases, these NFAs have primarily utilized thiophene or thiophene-based heterocycles, whereas selenophene-based NFAs have received much less attention.[3,4]

As a thiophene analogue, selenophene exhibits several attractive advantages.[26–30] Selenophene has stronger electron-donating ability and reduced aromaticity relative to thiophene, which could increase the quinoidal character of selenophene-based NFAs.[31] As a result, selenophene-based NFAs tend to exhibit improved planarity, an increased effective conjugation length, and a lower optical bandgap.[32–34] In addition, due to the larger size and greater polarizability of selenium in comparison to sulfur, selenophene has a tendency to induce intermolecular Se···Se (chalcogen interaction) or selenium–aromatic interactions in corresponding selenophene-based NFAs.[27,28]

The aforementioned desirable features of selenophene-based NFAs have resulted in increased research interest regarding their use in OSC applications.[32–36] For example, by incorporating selenophene into the main backbone of NFAs, Liao and co-workers reported a selenophene-containing acceptor IDSe-T-IC.[32] The OSCs based on J51:IDSe-T-IC showed a maximum PCE of 8.58% without any additive treatment, which was much higher than that of the J51:$PC_{71}BM$ devices (PCE = 6.0%). Meanwhile, the same group also reported a novel acceptor, IDTIDSe-IC, bearing a fused 10-heterocyclic ring with two selenium atoms in the main backbone.[33] The OSCs based on J51:IDTIDSe-IC exhibited a PCE of 8.02%, with a small driving force for hole transfer between J51 and IDTIDSe-IC. Subsequently, by using selenophene as the π bridge, Geng and co-workers developed a near-infrared-absorbing acceptor IDT2Se-4F, which exhibited a low optical bandgap of 1.39 eV.[35] The IDT2Se-4F-based OSCs achieved a high PCE up to 11.19% with a short-circuit current density (J_{sc}) of 21.49 mA cm^{-2}. Using selenophene as the π bridge to extend the extent of conjugation

[a]School of Chemistry, Beihang University, Beijing 100191, China. E-mail: sunym@buaa.edu.cn

[b]Department of Chemistry, College of Science, Korea University, Seoul 136-713, Republic of Korea. E-mail: hywoo@korea.ac.kr

† Electronic supplementary information (ESI) available. See DOI: 10.1039/c8ta11197a

‡ These two authors contributed equally to this work.

and enhance the backbone planarity *via* noncovalent O···Se interactions, Liu and co-workers reported a selenophene-containing acceptor IDTO-Se-4F, which showed strong light absorption between 600 and 900 nm.[34] By blending this acceptor with PBDB-T, the OSCs based on IDTO-Se-4F yielded a high PCE of 10.67% with a low energy loss of 0.57 eV. Using alkyl-substituted selenophene as a side chain, Yang and coworkers reported an alkylselenophenyl-substituted acceptor ITCPTC-Se.[36] A stronger σ-inductive effect between the selenophene side group and the electron-donating backbone endowed ITCPTC-Se with high optical absorption and increased the lowest unoccupied molecular orbital (LUMO) energy level. However, the OSCs based on ITCPTC-Se exhibited a PCE of 9.02%, which was much lower than that of its thiophene counterpart based OSCs (10.61%). Given the aforementioned results (Fig. 1), it can be concluded that OSCs based on selenophene-containing NFAs have usually been limited to relatively low PCEs and fill factors.

Recently, our group developed a novel molecular design strategy toward asymmetric NFAs *via* appropriately extending the conjugation of the central indacenodithiophene (IDT) backbone.[37–39] By fusing one thiophene moiety on only one side of the IDT unit, we were the first to develop an asymmetric TPTT central core unit and subsequently the corresponding asymmetric acceptor TPTT-IC.[37] Due to the asymmetric structure, three kinds of packing modes by terminal π–π stacking were found for TPTT-IC. Moreover, asymmetric TPTT-IC has stronger intermolecular interactions than symmetric ITIC as two intermolecular binding energies of the TPTT-IC dimer were higher than that of the symmetric ITIC dimer. Indeed, relative to symmetric ITIC, asymmetric TPTT-IC exhibited a higher electron mobility in neat film and higher and more balanced charge carrier transport in blend film. As a result, a decent PCE of 10.5% with a FF of 70% was achieved for TPTT-IC-based OSCs, slightly higher than those of ITIC-based OSCs. Subsequently, by fusing one thieno[3,2-*b*]thiophene on one side of the IDT unit, we synthesized an asymmetric TPTTT central core unit, which is an isomer of the IDTT unit, and reported an asymmetric acceptor TPTTT-2F.[38] After blending the acceptor with PBT1-C,[40] the OSCs based on TPTTT-2F demonstrated a high PCE of 12.03% with a FF approaching 74.5%. By fusing one thiophene and one thieno[3,2-*b*]thiophene on the two termini of the IDT unit, we also synthesized an asymmetric TTPTTT central core unit and a corresponding acceptor TTPTTT-4F.[39] The TTPTTT-4F-based OSC exhibited a PCE of up to 12.05% with a FF of 72.1%. These results demonstrate that rationally modulating the extent of conjugation in the central core is an effective method to design high-performance A–D–A-type NFAs for OSC applications.

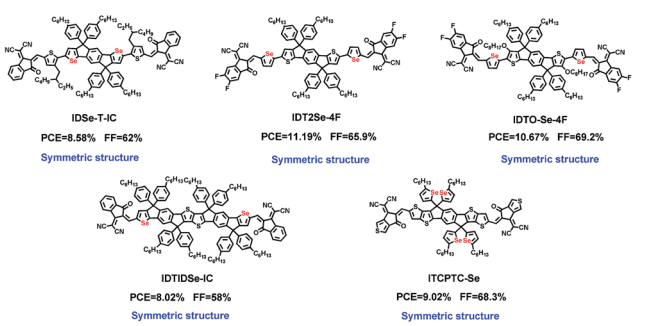

Fig. 1 Chemical structures of selenophene-based NFAs reported in the literature.

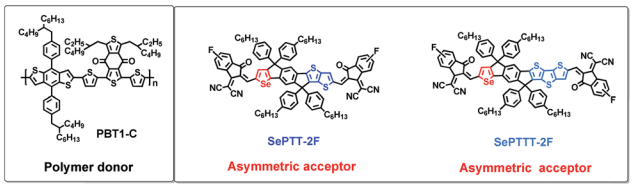

Fig. 2 Chemical structures of PBT1-C, SePTT-2F and SePTTT-2F.

In this contribution, in view of our recent studies and the potential advantages of selenophene over thiophene, we synthesized two selenophene-based building blocks, SePTT and SePTTT, in which the thiophene in the TPTT and TPTTT building blocks was replaced by selenophene. Using these two novel selenophene-containing building blocks as central cores, we then designed two asymmetric selenophene-containing NFAs named SePTT-2F and SePTTT-2F (Fig. 2), which have the same electron-withdrawing end-capping group but a different extent of conjugation in the selenophene-containing backbone. Both NFAs were found to exhibit strong and broad absorption from 550 to 850 nm and optical bandgaps of 1.50 eV in film. On the other hand, SePTTT-2F, which has more extended conjugation, was found to have an up-shifted LUMO energy level and improved electron mobility in comparison to SePTT-2F. The blend film based on the polymer donor PBT1-C[40] and SePTTT-2F exhibited higher and more balanced charge transport, enhanced exciton dissociation, and improved charge collection efficiency compared to the SePTT-based blend film. The OSCs based on PBT1-C:SePTTT-2F achieved a PCE of 12.24%, with an open-circuit voltage (V_{oc}) of 0.895 eV, a short-circuit current density (J_{sc}) of 18.02 mA cm^{-2} and a FF of 75.9%. These parameters were all higher than those of the SePTT-2F based OSCs with a PCE of 10.9%, a V_{oc} of 0.83 V, a J_{sc} of 17.51 mA cm^{-2} and a FF of 75%. To the best of our knowledge, the PCE of 12.24% and the FF of 75.9% are among the highest values reported in the literature so far for both the parameters amongst selenophene-containing NFA-based OSCs. Furthermore, the OSC device based on SePTTT-2F exhibited better thermal stability than the SePTT-2F-based OSC device, and an initial PCE of 96.3% could be maintained for the SePTTT-2F-based OSC device after thermal treatment at 100 °C for 8 h. Our results indicate that extending the extent of conjugation in the selenophene-containing backbone is an effective strategy to design highly efficient selenophene-containing A–D–A-type NFAs.

Results and discussion

The synthetic procedures for SePTT-2F and SePTTT-2F are depicted in Scheme 1, and details of their syntheses and structural characterizations can be found in the ESI.† A Stille

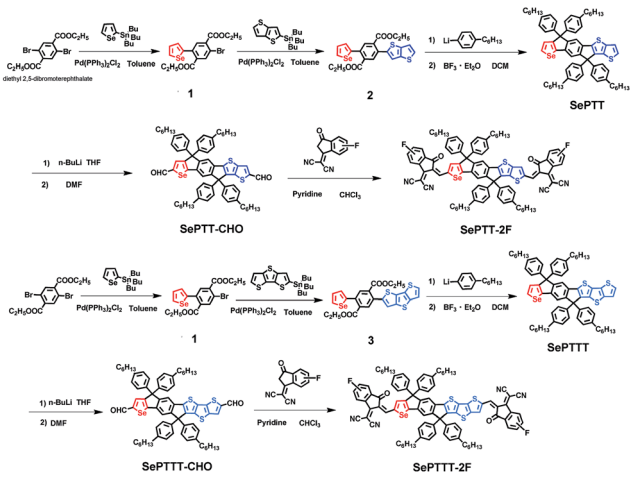

Scheme 1 Synthetic procedures for SePTT-2F and SePTTT-2F.

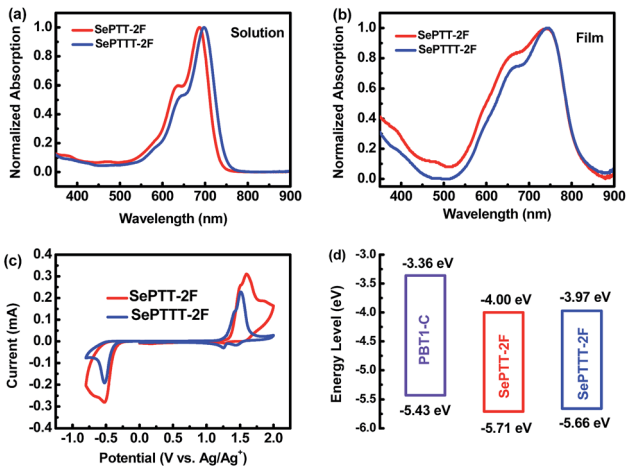

Fig. 3 Normalized absorption spectra of SePTT-2F and SePTTT-2F in (a) chloroform solution and (b) thin films. (c) Cyclic voltammograms of SePTT-2F and SePTTT-2F. (d) Energy level diagrams of PBT1-C, SePTT-2F and SePTTT-2F.

coupling reaction between diethyl 2,5-dibromoterephthalate and one molar equivalent of tributyl(selenophen-2-yl)stannane using $Pd(PPh_3)_2Cl_2$ as a catalyst afforded compound **1**, which was subsequently reacted with tributyl(thieno[3,2-*b*]thiophen-2-yl)stannane *via* a Stille coupling reaction to furnish compound **2**. Subsequently, compound **2** was reacted with (4-hexylphenyl) lithium *via* a nucleophilic addition to yield two benzyl alcohols, followed by a Friedel–Crafts reaction in the presence of BF_3 etherate to form the six-membered selenophene-containing asymmetric building block SePTT. This SePTT was then lithiated by *n*-butyllithium and quenched by anhydrous *N*,*N*-dimethylformamide (DMF) to afford the key intermediate SePTT-CHO. Finally, a Knoevenagel condensation reaction between SePTT-CHO and 2-(6-fluoro-3-oxo-2,3-dihydro-1*H*-inden-1-ylidene)malononitrile resulted in the formation of SePTT-2F.

SePTTT-2F, with extended backbone conjugation, could be synthesized *via* the same synthetic procedure used for SePTT-2F. The newly synthesized SePTT-2F and SePTTT-2F were fully characterized by ^{1}H NMR, ^{13}C NMR, and mass spectrometry (*e.g.*, matrix-assisted laser desorption ionization-time of flight (MALDI-TOF)). Both SePTT-2F and SePTTT-2F exhibited very good solubility in common organic solvents including dichloromethane, chloroform, and chlorobenzene at room temperature.

The normalized absorption spectra of SePTT-2F and SePTTT-2F are presented in Fig. 3. In dilute chloroform solution, similar absorption profiles were observed for the two NFAs. Maximum absorption peaks were found at 686 nm for SePTT-2F and 697 nm for SePTTT-2F. The red-shifted absorption of SePTTT-2F relative to that of SePTT-2F was due to the more extended backbone conjugation in SePTTT. In film, both NFAs exhibited red-shifted and broader absorption spectra relative to their corresponding solution spectra, which is indicative of more pronounced π–π intermolecular interactions in the solid state for both NFAs. Furthermore, in thin films, both NFAs exhibited intense absorption in the range of 550–850 nm and nearly the same maximum absorption peak at 743 nm. The thin film of each NFA exhibited the same absorption edge at 824 nm, which corresponds to an optical bandgap of 1.50 eV. The corresponding optical data are summarized in Table 1.

The electrochemical properties of SePTT-2F and SePTTT-2F were evaluated by cyclic voltammetry (CV) measurements. The onset oxidation potential of the ferrocene external standard was determined to be 0.43 V relative to Ag/AgCl (Fig. S1†), and the highest occupied molecular orbital (HOMO) and LUMO energy levels were then estimated according to the following equations: HOMO $= -(E_{ox} + 4.37)$ eV and LUMO $= -(E_{red} + 4.37)$ eV, where E_{ox} and E_{red} are the onset oxidation and reduction potentials relative to Ag/AgCl, respectively. As shown in Fig. 3c, the E_{ox} and E_{red} of SePTT-2F and SePTTT-2F were determined to be 1.34 and −0.37 and 1.29 and −0.40 V, respectively. The corresponding HOMO and LUMO energy levels were then calculated to be −5.71 and −4.00 eV for SePTT-2F and −5.66 and −3.97 eV for SePTTT-2F, respectively. Compared to SePTT-2F, SePTTT-2F exhibited a higher HOMO energy level due to the more electron-rich nature of SePTTT relative to SePTT as well as a higher LUMO energy level, even though both NFAs contain the same electron-withdrawing end-capping group. These results are consistent with those of our previous work.[38] The relatively higher LUMO energy level of SePTTT-2F in comparison to SePTT-2F would induce a higher V_{oc} in the OSC device based on the former. The energy level diagrams of PBT1-C, SePTT-2F and SePTTT-2F are presented in Fig. 3d, and the corresponding electrochemical data are summarized in Table 1.

To evaluate the photovoltaic characteristics of the two selenophene-based asymmetric NFAs, OSCs were fabricated based on an inverted device configuration of ITO/ZnO/PBT1-C:NFA/MoO_3/Ag. PBT1-C was used as the donor material owing to its complementary light absorption and appropriate energy levels matching with those of the two NFAs for exciton separation. Device processing conditions, such as the donor/acceptor (D/A) weight ratio and the amount of 1,8-diiodooctane (DIO) additive, were systematically investigated to optimize the photovoltaic performance. With chlorobenzene as the processing solvent, the optimal D/A weight ratios were found to be 1 : 0.9 for the PBT1-C:SePTT-2F device and 1 : 1.1 for the PBT1-C:SePTTT-2F device. After adding 0.3 vol% of the DIO additive,

Table 1 Optical and electrochemical properties of the two NFAs

NFA	$\lambda_{max}{}^{a}$ [nm]	$\lambda_{max}{}^{b}$ [nm]	$\lambda_{onset}{}^{b}$ [nm]	E_g^{optc} [eV]	E_{ox} [V]	HOMO [eV]	E_{red} [V]	LUMO [eV]
SePTT-2F	686	743	824	1.50	1.34	−5.71	−0.37	−4.00
SePTTT-2F	697	743	824	1.50	1.29	−5.66	−0.40	−3.97

[a] In $CHCl_3$ solution. [b] In a thin film drop cast from $CHCl_3$ solution. [c] Estimated from the empirical formula $E_g^{opt} = 1240/\lambda_{onset}$.

the best photovoltaic performance was achieved for both devices. As shown in Fig. 4 and Table 2, the optimized device based on SePTT-2F showed a PCE of 10.9% with a V_{oc} of 0.83 V, a J_{sc} of 17.51 mA cm^{-2}, and a FF of 75%. For the optimized device based on SePTTT-2F, an impressively high PCE of 12.24% was recorded with a V_{oc} of 0.895 V, a J_{sc} of 18.02 mA cm^{-2}, and a FF of 75.9%. The higher PCE of the SePTTT-2F-based device was attributed to simultaneous improvements in V_{oc},J_{sc}, and FF as compared with those of the SePTT-2F-based device. The relatively higher V_{oc} of the SePTTT-2F based device was in good accordance with the up-shifted LUMO energy level of SePTTT-2F relative to that of SePTT-2F. It is worth highlighting that the SePTT-2F-based device exhibited an impressively high FF (≥75%), which is among the highest values reported so far for selenophene-containing NFA-based OSC devices. The thermal stabilities of the OSC devices based on PBT1-C:SePTT-2F and PBT1-C:SePTTT-2F were also tested. As shown in Fig. S4,† the thermal stability of the PBT1-C:SePTT-2F-based device was lower than that of the device based on PBT1-C:SePTTT-2F. 96.3% of the initial PCE could be maintained for the PBT1-C:SePTTT-2F-based device after thermal treatment at 100 °C for 8 h, whereas for the PBT1-C:SePTT-2F-based device, after annealing at 100 °C for 8 h, only 78.9% of the initial PCE could be maintained. These results demonstrate that the device based on SePTTT-2F, with more extended conjugation in the selenophene-containing backbone, showed better thermal stability than the SePTT-2F-based device. The ambient stability of optimized OSC devices without encapsulation was also tested. As shown in Fig. S5,† both devices could retain over 90% of their initial PCE after 96 h under ambient conditions, indicating that the OSC devices based on asymmetric selenophene-based NFAs show excellent ambient stability.

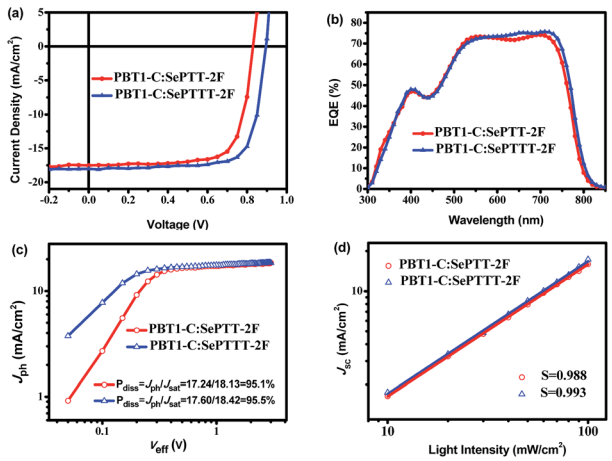

Fig. 4 (a) *J*–*V* curves and (b) EQE spectra of the optimized OSC devices based on the PBT1-C:NFA blend. A plot of (c) J_{ph} *versus* V_{eff} and (d) light intensity dependence of J_{sc} for the optimized OSC devices.

The external quantum efficiency (EQE) spectra of the optimized OSC devices are presented in Fig. 4b. Both OSC devices exhibited broad photoresponses over a broad range from 300 to 850 nm, with maximum EQE values of 75.6% at 714 nm for the SePTTT-2F-based OSC device and 74.4% at 700 nm for the SePTT-2F-based OSC device, suggesting that efficient charge generation and collection occurred in both OSC devices. The integrated J_{sc} obtained from the EQE spectra was determined to be 17.21 mA cm^{-2} for the SePTTT-2F-based device, which was slightly higher than the value of 16.72 mA cm^{-2} measured for the SePTT-2F based device, demonstrating that the SePTTT-2F-based device enabled a more efficient photoelectric conversion process than the SePTT-2F-based device. The integrated J_{sc} values are in good accordance with the J_{sc} values obtained from the *J*–*V* measurements, with a mismatch below 5%.

The charge transport properties of two neat films and the corresponding blend films based on both NFAs were studied using the space-charge-limited current (SCLC) method. As shown in Fig. S6† and Table S3,† the electron mobility (μ_e) of the neat SePTTT-2F film was measured to be 12.19 × 10^{-4} cm^2 V^{-1} s^{-1}, which was ~2 times higher than that of the neat SePTT-2F film (5.14 × 10^{-4} cm^2 V^{-1} s^{-1}). As for the blend films, the hole mobilities (μ_h) and electron mobilities of the PBT1-C:SePTT-2F and PBT1-C:SePTTT-2F blend films were determined to be 7.46 × 10^{-4} and 2.49 × 10^{-4} and 11.54 × 10^{-4} and 4.38 × 10^{-4} cm^2 V^{-1} s^{-1}, corresponding to the μ_h/μ_e ratios of 3.00 and 2.63, respectively. The SePTTT-2F blend film

Table 2 Photovoltaic data of the optimized OSCs based on PBT1-C:NFA

NFA	V_{oc} (V)	J_{sc} (mA cm^{-2})	$J_{sc,cal}$ (mA cm^{-2})	FF (%)	PCE[a] (%)
SePTT-2F	0.830 (0.829 ± 0.002)	17.51 (17.25 ± 0.27)	16.72	75.0 (74.5 ± 0.66)	10.90 (10.65 ± 0.16)
SePTTT-2F	0.895 (0.896 ± 0.002)	18.02 (17.62 ± 0.19)	17.21	75.9 (75.94 ± 0.35)	12.24 (11.99 ± 0.13)

[a] Average values with standard deviations were obtained from 20 devices.

exhibited higher and more balanced charge carrier mobility relative to the SePTT-2F blend film, which agrees well with the slightly higher J_{sc} and FF observed for the SePTTT-2F-based OSC device.

The exciton dissociation and charge collection properties were studied by measuring the photocurrent density (J_{ph}) against effective voltage (V_{eff}). As depicted in Fig. 4c, saturated J_{ph} (J_{sat}) values were achieved for both devices based on the blend films at a V_{eff} greater than 2 V, suggesting that all the photogenerated free charge carriers were collected by the electrodes. The J_{sat} value for the PBT1-C:SePTTT-2F device was 18.42 mA cm^{-2}, which was slightly higher than the J_{sat} value of 18.13 mA cm^{-2} for the PBT1-C:SePTT-2F-based device. Under short-circuit conditions, the exciton dissociation probability (P_{diss}) was evaluated by measuring the ratio of J_{ph}/J_{sat}. The P_{diss} values of the PBT1-C:SePTT-2F- and PBT1-C:SePTTT-2F-based devices were determined to be 95.1% and 95.5%, respectively, suggesting that the device based on SePTTT-2F had slightly more efficient exciton dissociation and charge collection efficiency than the SePTT-2F-based device.[41] The charge recombination behavior was also studied by measuring the J_{sc} as a function of light intensity (P_{light}). The relationship between J_{sc} and P_{light} is described by the formula $J_{sc} \propto P_{light}^{S}$, wherein the exponential factor S is an indicator of the extent of bimolecular recombination. A value of $S = 1$ represents the case wherein all free carriers are swept out and collected at the electrodes prior to recombination, while values of $S < 1$ indicate some degree of bimolecular recombination.[42] As shown in Fig. 4d, the S values of the PBT1-C:SePTT-2F- and PBT1-C:SePTTT-2F-based devices were determined to be 0.988 and 0.993, respectively, suggesting that negligible bimolecular charge recombination occurred in both blend devices.

The film morphology of the blend films was investigated using atomic force microscopy (AFM) and transmission electron microscopy (TEM). As can be seen from the AFM height and phase images shown in Fig. 5, a clear fiber network structure, which is beneficial for efficient charge transport,[40] was observed in both the PBT1-C:SePTT-2F and PBT1-C:SePTTT-2F blend films. Moreover, the AFM height images of both blend films showed relatively small root mean square roughness (RMS), with RMS values of 1.92 nm for the PBT1-C:SePTT-2F blend film and 2.04 nm for the PBT1-C:SePTTT-2F blend film. The fibrous features shown in the AFM phase images were more pronounced in the SePTTT-2F-based blend film than those in the SePTT-2F-based blend film. In the TEM images, a similar trend to the AFM measurements was observed: an interpenetrating network structure was observed in both blend films, demonstrating that favorable phase separation occurred between PBT1-C and the selenophene-containing asymmetric NFAs.

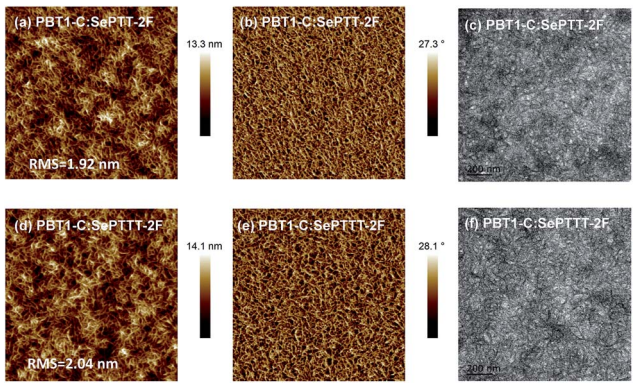

Fig. 5 (a and d) AFM height images, (b and e) AFM phase images, and (c and f) TEM images of the blend films.

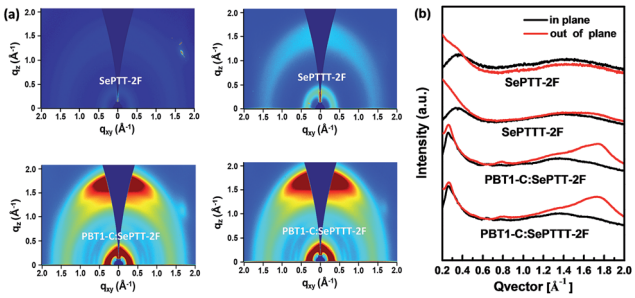

Fig. 6 (a) GIWAXS patterns of SePTT-2F and SePTTT-2F neat films and their corresponding blend films. (b) In-plane (black lines) and out-of-plane (red lines) line-cut profiles of the GIWAXS results.

The molecular orientation and packing behaviors of the two selenophene-based NFAs in both neat and blend films were studied *via* grazing incidence wide-angle X-ray scattering (GIWAXS) measurements. The GIWAXS patterns and corresponding line-cuts are illustrated in Fig. 6. For both SePTT-2F and SePTTT-2F neat films, negligible lamellar and π–π stacking scatterings were measured, suggesting that both neat films exhibited weak crystallinity. Regarding the blend films, as evidenced by a strong (100) scattering peak in the in-plane (IP) direction and a strong (010) scattering peak in the out-of-plane (OOP) direction, both PBT1-C:SePTT-2F and PBT1-C:SePTTT-2F blend films preferentially adopted face-on orientation relative to the substrate. In contrast to the π–π stacking peak at 1.61 Å^{-1} in the OOP direction and the lamellar stacking peak at 0.25 Å^{-1} for the neat PBT1-C film (Fig. S7†), the π–π stacking peaks in the OOP direction and lamellar stacking peaks in the IP direction were shifted to 1.72 Å^{-1} and 0.26 Å^{-1} (Fig. S8 and Table S4†), respectively, for both blend films, indicating tighter interchain packing (π–π stacking *d*-spacing of ~3.6 Å and lamellar *d*-spacing of ~24 Å, respectively) in the blends compared to the pristine PBT1-C film. Both the blend films showed similar GIWAXS scattering patterns with nearly identical packing structures, which show a good agreement with the optical, AFM/TEM morphological and photoelectrical characteristics.

Conclusions

In summary, two novel asymmetric selenophene-based A–D–A-type NFAs, SePTT-2F and SePTTT-2F, containing the same electron-withdrawing end-capping group but different extents of conjugation in the backbone, were designed and synthesized. In comparison with SePTT-2F, the SePTTT-2F, with extended

backbone conjugation, was found to have the same maximum absorption peak and optical bandgap in film but an up-shifted LUMO energy level and improved electron mobility. The OSCs based on PBT1-C:SePTTT-2F delivered an impressively high PCE of 12.24%, outperforming the SePTT-2F-based OSCs (PCE 10.9%), which was ascribed to simultaneous enhancements in V_{oc}, J_{sc}, and FF. It is worth noting that very high FF values ($\geq$75%) were obtained for OSCs based on these two asymmetric selenophene-based NFAs. The results demonstrate that these two asymmetric selenophene-based building blocks are promising central cores for use in the design of high-performance A–D–A-type NFAs.

Conflicts of interest

There are no conflicts to declare.

Acknowledgements

This work was financially supported by the National Natural Science Foundation of China (NSFC) (No. 21674007, 21734001, and 51825301). HYW acknowledges the financial support from the National Research Foundation (NRF) of Korea (2012M3A6A7055540 and 2015M1A2A2057506).

Notes and references

1 Y. Lin, J. Wang, Z.-G. Zhang, H. Bai, Y. Li, D. Zhu and X. Zhan, *Adv. Mater.*, 2015, **27**, 1170–1174.
2 H. Fu, Z. Wang and Y. Sun, *Angew. Chem., Int. Ed.*, 2018, DOI: 10.1002/anie.201806291.
3 F. Shen, J. Xu, X. Li and C. Zhan, *J. Mater. Chem. A*, 2018, **6**, 15433–15455.
4 D. He, F. Zhao, L. Jiang and C. Wang, *J. Mater. Chem. A*, 2018, **6**, 8839–8854.
5 G. Zhang, J. Zhao, P. C. Y. Chow, K. Jiang, J. Zhang, Z. Zhu, J. Zhang, F. Huang and H. Yan, *Chem. Rev.*, 2018, **118**, 3447–3507.
6 J. Hou, O. Inganäs, R. H. Friend and F. Gao, *Nat. Mater.*, 2018, **17**, 119.
7 C. Yan, S. Barlow, Z. Wang, H. Yan, A. K. Y. Jen, S. R. Marder and X. Zhan, *Nat. Rev. Mater.*, 2018, **3**, 18003.
8 S. Li, L. Ye, W. Zhao, H. Yan, B. Yang, D. Liu, W. Li, H. Ade and J. Hou, *J. Am. Chem. Soc.*, 2018, **140**, 7159–7167.
9 W. Zhao, S. Li, H. Yao, S. Zhang, Y. Zhang, B. Yang and J. Hou, *J. Am. Chem. Soc.*, 2017, **139**, 7148–7151.
10 W. Zhao, D. Qian, S. Zhang, S. Li, O. Inganäs, F. Gao and J. Hou, *Adv. Mater.*, 2016, **28**, 4734–4739.
11 Y. Cai, L. Huo and Y. Sun, *Adv. Mater.*, 2017, **29**, 1605437.
12 Z. Zhang and X. Zhu, *Chem. Mater.*, 2018, **30**, 587–591.
13 Z. Fei, F. D. Eisner, X. Jiao, M. Azzouzi, J. A. Röhr, Y. Han, M. Shahid, A. S. R. Chesman, C. D. Easton, C. R. McNeill, T. D. Anthopoulos, J. Nelson and M. Heeney, *Adv. Mater.*, 2018, **30**, 1705209.
14 S.-L. Chang, F.-Y. Cao, W.-C. Huang, P.-K. Huang, K.-H. Huang, C.-S. Hsu and Y.-J. Cheng, *ACS Energy Lett.*, 2018, **3**, 1722–1729.
15 C. Huang, X. Liao, K. Gao, L. Zuo, F. Lin, X. Shi, C.-Z. Li, H. Liu, X. Li, F. Liu, Y. Chen, H. Chen and A. K. Y. Jen, *Chem. Mater.*, 2018, **30**, 5429–5434.
16 S. Li, L. Zhan, F. Liu, J. Ren, M. Shi, C.-Z. Li, T. P. Russell and H. Chen, *Adv. Mater.*, 2018, **30**, 1705208.
17 H. Yao, L. Ye, J. Hou, B. Jang, G. Han, Y. Cui, G. M. Su, C. Wang, B. Gao, R. Yu, H. Zhang, Y. Yi, H. Y. Woo, H. Ade and J. Hou, *Adv. Mater.*, 2017, **29**, 1700254.
18 J. Wang, J. Zhang, Y. Xiao, T. Xiao, R. Zhu, C. Yan, Y. Fu, G. Lu, X. Lu, S. R. Marder and X. Zhan, *J. Am. Chem. Soc.*, 2018, **140**, 9140–9147.
19 Y. Yang, Z.-G. Zhang, H. Bin, S. Chen, L. Gao, L. Xue, C. Yang and Y. Li, *J. Am. Chem. Soc.*, 2016, **138**, 15011–15018.
20 R. Li, G. Liu, R. Xie, Z. Wang, X. Yang, K. An, W. Zhong, X.-F. Jiang, L. Ying, F. Huang and Y. Cao, *J. Mater. Chem. C*, 2018, **6**, 7046–7053.
21 D. Xie, T. Liu, W. Gao, C. Zhong, L. Huo, Z. Luo, K. Wu, W. Xiong, F. Liu, Y. Sun and C. Yang, *Sol. RRL*, 2017, **1**, 1700044.
22 H. Zhang, H. Yao, J. Hou, J. Zhu, J. Zhang, W. Li, R. Yu, B. Gao, S. Zhang and J. Hou, *Adv. Mater.*, 2018, **30**, 1800613.
23 B. Kan, H. Feng, X. Wan, F. Liu, X. Ke, Y. Wang, Y. Wang, H. Zhang, C. Li, J. Hou and Y. Chen, *J. Am. Chem. Soc.*, 2017, **139**, 4929–4934.
24 W. Gao, Q. An, C. Zhong, Z. Luo, R. Ming, M. Zhang, Y. Zou, F. Liu, F. Zhang and C. Yang, *Chem. Sci.*, 2018, **9**, 8142–8149.
25 X. Li, H. Huang, Z. Peng, C. Sun, D. Yang, J. Zhou, A. Liebman-Pelaez, C. Zhu, Z.-G. Zhang, Z. Zhang, Z. Xie, H. Ade and Y. Li, *J. Mater. Chem. A*, 2018, **6**, 15933–15941.
26 A. Patra and M. Bendikov, *J. Mater. Chem.*, 2010, **20**, 422–433.
27 R. S. Ashraf, I. Meager, M. Nikolka, M. Kirkus, M. Planells, B. C. Schroeder, S. Holliday, M. Hurhangee, C. B. Nielsen, H. Sirringhaus and I. McCulloch, *J. Am. Chem. Soc.*, 2015, **137**, 1314–1321.
28 F.-Y. Cao, C.-C. Tseng, F.-Y. Lin, Y. Chen, H. Yan and Y.-J. Cheng, *Chem. Mater.*, 2017, **29**, 10045–10052.
29 Z. Zhao, Z. Yin, H. Chen, L. Zheng, C. Zhu, L. Zhang, S. Tan, H. Wang, Y. Guo, Q. Tang and Y. Liu, *Adv. Mater.*, 2017, **29**, 1602410.
30 J. J. Intemann, K. Yao, H.-L. Yip, Y.-X. Xu, Y.-X. Li, P.-W. Liang, F.-Z. Ding, X. Li and A. K. Y. Jen, *Chem. Mater.*, 2013, **25**, 3188–3195.
31 Z. Fei, Y. Han, E. Gann, T. Hodsden, A. S. R. Chesman, C. R. McNeill, T. D. Anthopoulos and M. Heeney, *J. Am. Chem. Soc.*, 2017, **139**, 8552–8561.
32 Y. Li, L. Zhong, F.-P. Wu, Y. Yuan, H.-J. Bin, Z.-Q. Jiang, Z. Zhang, Z.-G. Zhang, Y. Li and L.-S. Liao, *Energy Environ. Sci.*, 2016, **9**, 3429–3435.
33 Y. Li, D. Qian, L. Zhong, J.-D. Lin, Z.-Q. Jiang, Z.-G. Zhang, Z. Zhang, Y. Li, L.-S. Liao and F. Zhang, *Nano Energy*, 2016, **27**, 430–438.
34 D. Liu, B. Kan, X. Ke, N. Zheng, Z. Xie, D. Lu and Y. Liu, *Adv. Energy Mater.*, 2018, **8**, 1801618.
35 Z. Liang, M. Li, X. Zhang, Q. Wang, Y. Jiang, H. Tian and Y. Geng, *J. Mater. Chem. A*, 2018, **6**, 8059–8067.
36 W. Gao, Q. An, R. Ming, D. Xie, K. Wu, Z. Luo, Y. Zou, F. Zhang and C. Yang, *Adv. Funct. Mater.*, 2017, **27**, 1702194.

37 C. Li, Y. Xie, B. Fan, G. Han, Y. Yi and Y. Sun, *J. Mater. Chem. C*, 2018, **6**, 4873–4877.
38 J. Song, C. Li, L. Ye, C. Koh, Y. Cai, D. Wei, H. Y. Woo and Y. Sun, *J. Mater. Chem. A*, 2018, **6**, 18847–18852.
39 C. Li, J. Song, L. Ye, C. Koh, K. Weng, H. Fu, Y. Cai, Y. Xie, D. Wei, H. Y. Woo and Y. Sun, *Sol. RRL*, 2018, DOI: 10.1002/solr.201800246.
40 T. Liu, L. Huo, S. Chandrabose, K. Chen, G. Han, F. Qi, X. Meng, D. Xie, W. Ma, Y. Yi, J. M. Hodgkiss, F. Liu, J. Wang, C. Yang and Y. Sun, *Adv. Mater.*, 2018, **30**, 1707353.
41 S. Dai, T. Li, W. Wang, Y. Xiao, T.-K. Lau, Z. Li, K. Liu, X. Lu and X. Zhan, *Adv. Mater.*, 2018, **30**, 1706571.
42 I. Riedel, J. Parisi, V. Dyakonov, L. Lutsen, D. Vanderzande and J. C. Hummelen, *Adv. Funct. Mater.*, 2004, **14**, 38–44.